GEOPHYSICS, VOL. 84, NO. 2 (MARCH-APRIL 2019); P. S95–S111, 18 FIGS., 1 TABLE.
10.1190/GEO2018-0197.1

Imaging conditions for elastic reverse time migration

Wei Zhang[1] and Ying Shi[1]

ABSTRACT

Elastic reverse time migration (RTM) has the ability to retrieve accurately migrated images of complex subsurface structures by imaging the multicomponent seismic data. However, the imaging condition applied in elastic RTM significantly influences the quality of the migrated images. We evaluated three kinds of imaging conditions in elastic RTM. The first kind of imaging condition involves the crosscorrelation between the Cartesian components of the particle-velocity wavefields to yield migrated images of subsurface structures. An alternative crosscorrelation imaging condition between the separated pure wave modes obtained by a Helmholtz-like decomposition method could produce reflectivity images with explicit physical meaning and fewer crosstalk artifacts. A drawback of this approach, though, was that the polarity reversal of the separated S-wave could cause destructive interference in the converted-wave image after stacking over multiple shots. Unlike the conventional decomposition method, the elastic wavefields can also be decomposed in the vector domain using the decoupled elastic wave equation, which preserves the amplitude and phase information of the original elastic wavefields. We have developed an inner-product imaging condition to match the vector-separated P- and S-wave modes to obtain scalar reflectivity images of the subsurface. Moreover, an auxiliary P-wave stress image can supplement the elastic imaging. Using synthetic examples with a layered model, the Marmousi 2 model, and a fault model, we determined that the inner-product imaging condition has prominent advantages over the other two imaging conditions and generates images with preserved amplitude and phase attributes.

INTRODUCTION

With the improvement of computation capacity and acquisition technology, elastic imaging (Yan and Sava, 2008; Du et al., 2017), and inversion (Feng and Schuster, 2017; Wang et al., 2018a) with multicomponent seismic data has already become increasingly feasible. Elastic imaging has the capability of providing more opportunities in understanding the subsurface through reflection images associated with S-waves (e.g., PS, SP, and SS images) as compared with acoustic imaging with single-component seismic data. Assuming no attenuation in the subsurface, the converted-wave images also have a higher resolution than the P-wave images because the converted waves have shorter wavelengths (Yan and Sava, 2008).

Similar to the acoustic imaging technique, the elastic imaging technique includes three kinds of schemes: ray-based migrations (Kuo and Dai, 1984; Hokstad, 2000), one-way wave-equation migrations (Wu, 1994; Xie and Wu, 2005), and elastic reverse time migration (RTM) (Chang and McMechan, 1987, 1994). Among these elastic migration schemes, elastic RTM, which uses the two-way elastic wave equation for the propagation of elastic wavefields, is capable of accurately repositioning various kinds of seismic events (e.g., scattering, prismatic, and converted waves) into their actual geologic position in the subsurface and has no dip-angle limitation. For these reasons, elastic RTM is the most promising migration algorithm for multicomponent seismic data in complex geologic conditions.

Elastic RTM was initially performed by Sun and McMechan (1986) for elastic seismic data recorded in vertical seismic profiles. Chang and McMechan (1987, 1994) implement 2D and 3D elastic RTM for multicomponent seismic data based on the excitation-time imaging condition (Chang and McMechan, 1986). However, in their imaging algorithm, the scattered P- and S-waves are imaged simultaneously, which produces subsurface images with unclear physical meaning and serious crosstalk artifacts created by the unseparated wave modes.

Manuscript received by the Editor 17 March 2018; revised manuscript received 9 November 2018; published ahead of production 08 December 2018; published online 07 March 2019.
[1]Northeast Petroleum University, School of Earth Science, Daqing 163318, China. E-mail: zhangwei_geo@sina.com; shiying@nepu.edu.cn (corresponding author).

To decrease the crosstalk artifacts and make the images characterize explicit physical meaning, there are two practical RTM schemes used to migrate elastic seismic events. One is the scalar RTM for elastic seismic data implemented by Sun and McMechan (2001). This scheme first requires decomposition of the elastic seismic data recorded at the earth's surface into the P- and S-wave components, and then two scalar RTMs are implemented to reposition the separated data using a respective migration velocity model. Although the mature scalar RTM technique with the separated P- and S-waves data can produce subsurface images that clearly describe the reflectivity of the pure wave modes at physical property interfaces, there are two issues in this procedure that require further investigation. One is that the separation of multicomponent seismic data recorded at the earth's surface is often imperfect and may induce potential artifacts because of the lack of the vertical partial derivative. Another is that the scalar RTM does not accurately cope with the converted relationship of the wave modes and neglects the vector essence of the elastic wavefields.

Another practical scheme separates the extrapolated elastic wavefields into pure P- and S-wave modes by the Helmholtz-like decomposition method before implementing an imaging condition (Yan and Sava, 2008; Du et al., 2012; Duan and Sava, 2015; Li et al., 2016; Wang et al., 2017), in which the decomposition method can be carried out by computing the divergence and curl of the extrapolated elastic wavefields in the isotropic case. This scheme is theoretically superior to the scalar RTM scheme because these constructed source and receiver wavefields using the full elastic wave equation are capable of characterizing the propagation of the elastic wavefields in elastic earth media very well. It not only correctly accounts for the wave-mode conversion and keeps the vector characteristics of the input multicomponent seismic data, but it also effectively avoids the crosstalk artifacts by using the wavefield-decomposition method.

Nevertheless, this scheme still has two drawbacks. One is that the converted-wave image undergoes a polarity-reversal problem, which can lead to destructive interference when stacking multiple shots (Du et al., 2012). Additionally, in the 3D case, only if the 3C S-wave separated by the curl operator is scalarized (Du et al., 2014; Gong et al., 2018), the scalar reflection images associated with S-waves (e.g., PS, SP, and SS images) can be constructed by the conventional crosscorrelation imaging condition. There are some approaches to correct the polarity-reversal problem in the common-source domain (Du et al., 2012; Duan and Sava, 2015; Li et al., 2016; Wang et al., 2017) and in the angle domain (Rosales and Rickett, 2001; Rosales et al., 2008). Unfortunately, these correction approaches in the common-source domain frequently rely on the propagation directions calculated by the Poynting vector or polarization vector in the time-space domain, which will become invalid when complex multipathings are involved (Ren et al., 2017). Although other straightforward correction schemes realized in the angle domain are more precise than those in the common-source domain, they rely on complicated angle-decomposition procedures and have a high computational cost. Consequently, without great effort toward overcoming this unfavorable factor, it is difficult to obtain a satisfactory converted-wave image. Another drawback in this scheme is that the conventional wavefield decomposition approach by calculating the divergence and curl operators involves the spatial derivatives on the displacement or particle-velocity components, which will lead to a $\pi/2$ phase shift (Sun et al., 2001). Moreover, the amplitudes of the separated P- and S-waves are changed by $1/V_P$ and $1/V_S$ (V_P is the P-velocity and V_S is the S-velocity), respectively (Sun et al., 2011). Therefore, we must correct these separated waves before applying an imaging condition to obtain accurate angle-dependent image amplitudes.

Recently, a novel decoupled elastic wave equation proposed by Ma and Zhu (2003) has been extensively used in elastic RTM (Xiao and Leaney, 2010; Zhang and McMechan, 2011; Gu et al., 2015; Wang and McMechan, 2015; Gong et al., 2016). According to the Helmholtz decomposition theory (Aki and Richards, 1980), the conventional coupled elastic wave equation can be decomposed into P- and S-wave component equations, which together are called the decoupled elastic wave equation. These two equations can accurately describe the decoupled P- and S-wave propagation, which retains the vector feature of the input elastic wavefields. According to Ma and Zhu's (2003) derivations, Zhang et al. (2007) construct a decoupled version of Virieux's (1986) staggered-grid stress-velocity formulation, in which the particle velocities of the P- and S-waves are solved simultaneously. Xiao and Leaney (2010) also introduce the auxiliary P- and S-wave stresses to decompose the coupled elastic wavefields in the vector domain.

Unlike the conventional Helmholtz-like decomposition method that uses the divergence and curl operators, a valuable advantage of the decoupled elastic wave equation is that it can accurately preserve the amplitude and phase information of the input elastic wavefields. However, because the output wavefields from the decoupled elastic wave equation are both vectorial, a special imaging condition needs to be developed to exploit these decoupled vector wavefields as the input to generate reflection images with physically correct amplitudes. Wang and McMechan (2015) propose a modified excitation-amplitude imaging condition to implement the vector-based elastic RTM. The polarity assignment of the image amplitudes is necessarily required during the implementation of the imaging condition when the incident and reflected angles are known. According to the decoupled version of the stress-velocity formulation (Zhang et al., 2007), Gu et al. (2015) apply the crosscorrelation imaging condition between the Cartesian components of the decoupled particle-velocity wavefields to yield the coordinate-dependent images.

In this paper, we evaluated three kinds of imaging conditions in elastic RTM. The first one involved the zero-lag crosscorrelation between the horizontal or vertical components of the particle-velocity wavefields, which we refer to as the component-based imaging condition. Second, we performed the zero-lag crosscorrelation between the separated pure wave modes obtained by computing the divergence and curl of the particle-velocity wavefields, which we refer to as the potential-based imaging condition. For this imaging condition, we resolve the well-known polarity-reversal issue of the converted-wave image in the common-source domain. Finally, we have developed an inner-product imaging condition between the vector-separated pure waves from the decoupled elastic wave equation to produce scalar subsurface images.

THEORY OF ELASTIC REVERSE TIME MIGRATION

Prestack elastic RTM mainly consists of three steps: (1) Reconstruct the source elastic wavefield forward in time at a given physical source location, (2) reconstruct the receiver elastic wavefield backward in time by using the recorded multicomponent seismic data on the acquisition surface as boundary conditions, and (3) implement

an imaging condition to extract the subsurface reflectivity information from the reconstructed source and receiver wavefields.

The stress-velocity formulation of the elastodynamic equations in 2D isotropic media describing the propagation of the elastic vector wavefield is given by Virieux (1986)

$$\begin{aligned}
\frac{\partial \tau_{xx}}{\partial t} &= (\lambda + 2\mu)\frac{\partial v_x}{\partial x} + \lambda \frac{\partial v_z}{\partial z},\\
\frac{\partial \tau_{zz}}{\partial t} &= (\lambda + 2\mu)\frac{\partial v_z}{\partial z} + \lambda \frac{\partial v_x}{\partial x},\\
\frac{\partial \tau_{xz}}{\partial t} &= \mu\left(\frac{\partial v_z}{\partial x} + \frac{\partial v_x}{\partial z}\right),\\
\rho \frac{\partial v_x}{\partial t} &= \frac{\partial \tau_{xx}}{\partial x} + \frac{\partial \tau_{xz}}{\partial z},\\
\rho \frac{\partial v_z}{\partial t} &= \frac{\partial \tau_{zz}}{\partial z} + \frac{\partial \tau_{xz}}{\partial x},
\end{aligned} \tag{1}$$

where v_x and v_z are the horizontal and vertical components of the particle velocity, respectively, τ_{xx} and τ_{zz} are the normal stresses along the horizontal and vertical directions, respectively, τ_{xz} is the component of the shear stress, λ and μ are the Lamé parameters, ρ is the density, and t is the time. All elastic wavefield extrapolations in the modeling and migration in the synthetic examples below are performed by solving equation 1. We implemented the numerical solution of this equation by using a 12th order in space, 2nd order in time, staggered-grid finite-difference scheme. The artificial reflections from the boundaries can be suppressed by using a perfectly matched layer absorbing boundary condition (Berenger, 1994).

Imaging conditions in elastic RTM

A critical component for RTM is the imaging condition, which evaluates the match between the source and receiver wavefields. The type of imaging condition applied strongly influences the image amplitudes, physical validity, and resolution (Chattopadhyay and McMechan, 2008). There are three main classes of schemes: the excitation-time imaging condition (Chang and McMechan, 1986; Lowenthal and Hu, 1991), the excitation-amplitude imaging condition (Nguyen and McMechan, 2013, 2015), and the crosscorrelation imaging condition (or source normalized) (Kaelin and Guitton, 2006; Schleicher et al., 2008; Shi and Wang, 2016). Among these imaging conditions, the source-normalized crosscorrelation imaging condition has more advantages, which include better imaging quality at the deeper reflectors and reliable image amplitudes that represent the reflectivity of the mode with the correct scaling and sign. For these reasons, we only considered the source-normalized crosscorrelation imaging condition and its variants in elastic RTM.

Yan and Sava (2008) review various elastic imaging conditions, including imaging with vector displacement components and imaging with scalar and vector potentials. They concluded that migrated images constructed with the potential-based imaging condition were easier to interpret for physical properties than the component-based images because the former described the reflectivity of specified wave modes at physical property interfaces. Nevertheless, in the potential-based imaging condition, the separated wavefields from the Helmholtz-like decomposition method have altered the amplitude and phase of the input elastic wavefields. Furthermore, the polarity reversal of the separated S-wave could destroy the events of the converted-wave image. Motivated by Yan and Sava's (2008) works, we further explored and evaluated three elastic imaging conditions in elastic RTM: imaging with the vector particle-velocity wavefields, imaging with scalar and vector potentials from the Helmholtz-like decomposition method, and a proposed imaging condition, which involved the inner product between the vector-separated waves of the source and receiver wavefields from the decoupled elastic wave equation.

Imaging with the vector velocity wavefields

The imaging principle proposed by Claerbout (1971) states that a subsurface reflector can be mapped by the zero-lag crosscorrelation of a downgoing (source) wavefield and an upgoing (receiver) wavefield in a common-source gather. In elastic media, when the source and receiver elastic wavefields are available, a simple and natural component-by-component crosscorrelation between the two wavefields (e.g., the particle velocity) is able to retrieve the images of the subsurface structures. The source-normalized crosscorrelation imaging conditions for 2D images of the particle-velocity wavefields, for a common-source gather, can be formulated mathematically as

$$I_{xx}(x,z) = \frac{\sum_{it=1}^{nt} S_{vx}(x,z,it) R_{vx}(x,z,it)}{\sum_{it=1}^{nt} S_{vx}^2(x,z,it)} \tag{2}$$

and

$$I_{zz}(x,z) = \frac{\sum_{it=1}^{nt} S_{vz}(x,z,it) R_{vz}(x,z,it)}{\sum_{it=1}^{nt} S_{vz}^2(x,z,it)}, \tag{3}$$

where $S_{vx}(x,z,t)$ and $S_{vz}(x,z,t)$ are the horizontal and vertical components of the particle velocity for the source wavefield, $R_{vx}(x,z,t)$ and $R_{vz}(x,z,t)$ are the horizontal and vertical components of the particle velocity for the receiver wavefield, nt is the maximum number of time steps, and I_{xx} and I_{zz} represent the horizontal- and vertical-component images, respectively. We refer to the two equations as the component-based imaging condition.

Although the component-based imaging condition is easy to calculate, the resulting migration images have unclear physical meaning and are difficult to interpret for physical properties. Furthermore, the main drawback of this condition is that the migration images are subject to serious crosstalk artifacts because the unseparated P- and S-wave modes coupled in the particle-velocity wavefields are imaged simultaneously.

Imaging with scalar and vector potentials

To overcome those shortcomings in the component-based imaging condition, a practical algorithm proposed by Yan and Sava (2008) first decomposed the extrapolated elastic vector wavefields before the application of the imaging condition, and then crosscorrelated the separated pure P- and S-wave modes from the source and receiver wavefields. To produce the angle-domain common-image gathers from the elastic RTM, they discuss the extended elastic imaging conditions. Here, we preferred to implement the zero-lag crosscorrelation imaging condition. The source-normalized crosscorrelation imaging conditions for 2D PP and PS imaging, for a common-source gather, are given by Nguyen and McMechan (2015)

$$I_{\mathrm{PP}}(x,z) = \frac{\sum_{it=1}^{nt} S_{\nabla}(x,z,it) R_{\nabla}(x,z,it)}{\sum_{it=1}^{nt} S_{\nabla}^2(x,z,it)} \tag{4}$$

and

$$I_{\mathrm{PS}}(x,z)=\frac{\sum_{it=1}^{nt}S_{\nabla}(x,z,it)R_{\times}(x,z,it)}{\sum_{it=1}^{nt}S_{\nabla}^{2}(x,z,it)}, \tag{5}$$

where $S_{\nabla}(x,z,t)$ is the divergence of the particle velocity for the source wavefield, $R_{\nabla}(x,z,t)$ is the divergence of the particle velocity for the receiver wavefield, $R_{\times}(x,z,t)$ is the curl of the particle velocity for the receiver wavefield, and I_{PP} and I_{PS} represent the PP and PS reflection images, respectively. We refer to the two equations as the potential-based imaging condition.

The main advantage of this imaging condition is that it is capable of retrieving images of the subsurface structures with explicit physical meaning and fewer crosstalk artifacts compared with the component-based imaging condition. However, in the 3D case, it is impossible to directly construct the scalar PS reflection image from the potential-based imaging condition (equation 5) because the S-wave separated by the curl operator is a 3C vector and the P-wave separated by the divergence operator is a scalar quantity. In the 2D case, the separated S-wave ($R_{\times}$ in equation 5) can be considered a scalar quantity used in the elastic imaging, but the polarity reversal of the separated S-wave can degrade the migration quality when multiple shot PS images are stacked. The Helmholtz decomposition theory (Aki and Richards, 1980) states that the elastic wavefield (e.g., the receiver wavefield R) can be decomposed into a curl-free P-wave wavefield (R_P) and a divergence-free S-wave wavefield (R_S). Therefore, the S-wave wavefield can be separated by calculating the curl operator of the elastic wavefield, which can be written as

$$S=\nabla\times R=\nabla\times R_S, \tag{6}$$

where S represents the separated S-wave of the receiver wavefield, which is equal to $R_{\times}$ in equation 5, and R_S represents the original S-wave of the receiver wavefield. It is apparent from the equation that the separated S-wave does not keep the amplitude and phase information of the original wavefield. We transform equation 6 to the wavenumber domain, which produces the following equation (Du et al., 2012):

$$\tilde{S}=\frac{k_S}{|k_S|}\times\tilde{R}_S, \tag{7}$$

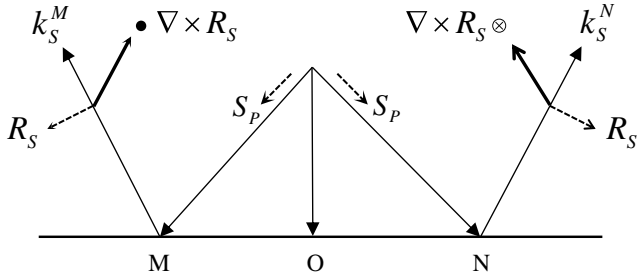

Figure 1. The polarity reversal of the S-wave separated by the curl operator. The values k_S^M and k_S^N represent the propagation directions of the reflected S-wave at points M and N, the dotted lines denote the vibration directions for the corresponding waves, S_P denotes the P-wave of the source wavefield, R_S denotes the S-wave of the receiver wavefield, and O is the normal-incidence point of the P-wave. According to the right-hand rule, the separated S-wave has an opposite polarity distribution at the two sides of the normal-incidence point of the P-wave. For example, the symbols • and ⊗ represent the two opposite polarity directions at points M and N, respectively.

where $\tilde{S}$ and $\tilde{R}_S$ denote the Fourier transforms of S and R_S along the spatial directions, respectively, and k_S denotes the wavenumber vector in the S-wave propagation direction. In the isotropic case, the vibration direction of the original S-wave is perpendicular to its propagation direction k_S. It is apparent from equation 7 that the separated S-wave is orthogonal to the plane constructed by the propagation and vibration directions. In Figure 1, we explain the essence of the polarity reversal of the separated S-wave at a horizontal reflector, in which O represents the normal-incidence point of the P-wave, and k_S^M and k_S^N represent the propagation directions of the reflected S-wave at points M and N, respectively. According to the right-hand rule, the separated S-wave has an opposite polarity distribution at the two sides of the normal-incidence point of the P-wave. For example, the symbols • and ⊗ represent the two opposite polarity directions at points M and N, respectively, which are displayed in Figure 1. The separated P-wave (S_{∇} in equation 5) is a scalar quantity without the polarity-reversal problem. Therefore, the PS reflection image constructed by equation 5 has an opposite sign distribution at the two sides of the normal-incidence point of the P-wave, which is the polarity-reversal problem of the PS reflection image.

Based on the previous explanation of the polarity reversal for the separated S-wave, the polarity reversal of the PS reflection image can be corrected by the estimated P-wave incident angle in the common-source domain. The correction formulas are expressed as

$$I_{\mathrm{PS}}(x,z)=\frac{\sum_{it=1}^{nt}S_{\nabla}(x,z,it)R_{\times}(x,z,it)[\text{sign of }\theta_P(x,z,it)]}{\sum_{it=1}^{nt}S_{\nabla}^{2}(x,z,it)}, \tag{8}$$

where sign of θ_P denotes the sign of a function and $\theta_P(x,z,it)$ denotes the P-wave incident angle at every grid and time step, which is produced as the difference between the propagation angle and the local angle of the reflector. The propagation angle can be efficiently estimated by the direction-vector-based method in the space-time domain (Jin et al., 2015). In this paper, we use the polarization direction of the P-wave to estimate the propagation angle (Zhang and McMechan, 2011), which can be written as

$$\alpha=\tan^{-1}\left(\frac{\frac{\partial}{\partial x}S_{\nabla}}{\frac{\partial}{\partial z}S_{\nabla}}\right), \tag{9}$$

where α denotes the P-wave propagation angle and the spatial partial derivatives represent the P-wave polarization direction. A limitation of the polarization direction is that it can only estimate a primary propagation direction at every grid in the time-space domain for overlapping events, so a least-squares solution along the spatial directions is exploited to enhance its accuracy in this paper (Yan and Dickens, 2016). We use the instantaneous wavenumber direction of the PP migration image to estimate the local angle of the reflector β (Zhang and McMechan, 2011). Hence, the P-wave incident angle is obtained as the difference between the propagation angle and the local angle of the reflector, which obeys the equation $\theta_P=\alpha-\beta$.

Although the polarity-reversal correction approach (equation 8) for the potential-based imaging condition can improve the imaging quality of the PS image, it is only suitable for simple geologic structures because this approach uses the estimated propagation direction from the polarization direction in the space-time domain, which will become unreliable when complex multipathings are involved.

Furthermore, the imaging condition involves the application of the divergence and curl operators to decompose the elastic wavefields, which leads to the amplitude and phase distortions of the elastic wavefields. Consequently, there is a need for correcting the separated waves of the potential-based imaging condition to obtain accurate angle-dependent image amplitudes.

Imaging with the vector P- and S-wave velocity wavefields

Unlike the conventional decomposition approach using the curl and divergence operators, the coupled elastic wavefields can also be decomposed in the vector domain using the decoupled elastic wave equation. Hence, the amplitude and phase information of the input elastic wavefields is automatically preserved. An auxiliary P-wave stress, which is a scalar wavefield, is introduced to achieve the wavefield decomposition process. This process of vector decomposition can be implemented by using the following equation (Wang et al., 2015):

$$\begin{aligned}
\frac{\partial \tau^P}{\partial t} &= (\lambda + 2\mu)\left(\frac{\partial v_x}{\partial x} + \frac{\partial v_z}{\partial z}\right),\\
\frac{\partial v_x^P}{\partial t} &= \frac{1}{\rho}\frac{\partial \tau^P}{\partial x},\\
\frac{\partial v_z^P}{\partial t} &= \frac{1}{\rho}\frac{\partial \tau^P}{\partial z},\\
v_x^S &= v_x - v_x^P,\\
v_z^S &= v_z - v_z^P,
\end{aligned} \tag{10}$$

where τ^P is the auxiliary P-wave stress, v_x^P and v_z^P are the horizontal and vertical components of the P-wave particle velocity, and v_x^S and v_z^S are the horizontal and vertical components of the S-wave particle velocity, respectively. This equation can also be solved using the same staggered-grid finite-difference approach as equation 1. The two equations accurately describe the decoupled P- and S-wave propagation, which together are called the decoupled elastic wave equation. When the coupled elastic wavefields are extrapolated by numerically solving equation 1, the P- and S-waves vector decomposition process requires three consecutive steps: (1) Compute the auxiliary P-wave stress via the horizontal and vertical components of particle velocity, (2) compute the vector-decomposed P-wave particle velocity from the computational auxiliary P-wave stress, and (3) obtain the vector-decomposed S-wave particle velocity via subtracting the P-wave particle velocity from the horizontal and vertical components of particle velocity.

Because these separated P- and S-waves are vectorial components, the type of imaging condition used plays an important role in repositioning these vector-separated pure waves to produce images with the correct amplitudes and physical meaning. Gu et al. (2015) apply the crosscorrelation imaging condition between the Cartesian components of the vector-separated waves to obtain the coordinate-dependent images (e.g., PPx, PPz, SSx, and SSz images). However, these images did not agree with our understanding of seismic reflectivity. To overcome this limitation, an inner product imaging condition for the vector-separated wave modes is proposed to produce scalar reflectivity images of the subsurface. The source-normalized inner-product imaging conditions for 2D PP and PS imaging, for a common-source gather, can be formulated mathematically as

$$I_{\mathrm{PP}}(x,z) = \frac{\sum_{it=1}^{nt} S_P(x,z,it)\cdot R_P(x,z,it)}{\sum_{it=1}^{nt} S_P(x,z,it)\cdot S_P(x,z,it)} \tag{11}$$

and

$$I_{\mathrm{PS}}(x,z) = \frac{\sum_{it=1}^{nt} S_P(x,z,it)\cdot R_S(x,z,it)}{\sum_{it=1}^{nt} S_P(x,z,it)\cdot S_P(x,z,it)}, \tag{12}$$

where the $\cdot$ symbol denotes the inner-product of two vectors, S_P and R_P denote the vector-separated P-wave of the source and receiver wavefields, respectively, and R_S denotes the vector-separated S-wave of the receiver wavefield.

Compared with the potential-based imaging condition (equations 4, 5, and 8), the inner-product imaging condition is capable of retrieving subsurface reflectivity images with better amplitude performance, which can be attributed to the amplitude-preserving wavefield decomposition approach with the decoupled elastic wave equation. The signs of the PP and PS reflection images can be determined from the principle that the incident and reflected waves have the same polarity for a negative reflection coefficient, and they have opposite polarity for a positive reflection coefficient (Aki and Richards, 1980; Wang and McMechan, 2015). When the PP and PS reflection coefficients are positive, Figure 2 displays the geometric relations among the propagation and vibration directions of the P- and S-waves in a reflector layer. Therefore, we can obtain the physical meaning interpretations of our inner-product imaging condition:

- For equation 11, the numerator for the PP reflection image can be transformed into $S_P\cdot R_P = |S_P||R_P|\cos(180°-2\theta_P) = -|S_P||R_P|\cos(2\theta_P)$, where θ_P denotes the P-wave incident angle. We can easily determine that the sign of the PP reflection image constructed with equation 11 depends on the

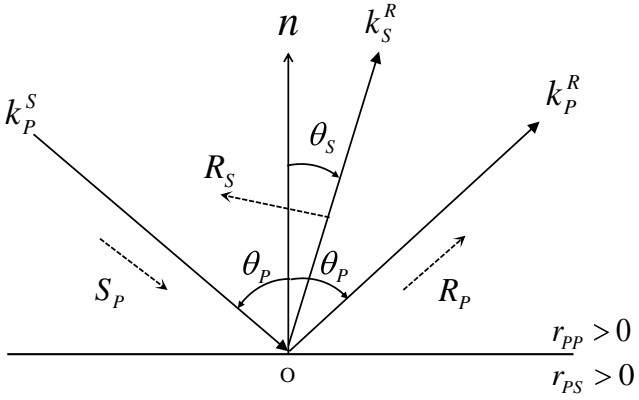

Figure 2. The geometric relations among the propagation and vibration directions of P- and S-waves in isotropic elastic media, assuming that the PP and PS reflection coefficients (r_{PP} and r_{PS}) are positive. k_P^S, k_P^R, and k_S^R indicate the propagation directions of the incident P-wave for the source wavefield, the reflected P-wave, and the converted S-wave for the receiver wavefield, respectively; the dotted lines denote the vibration directions for the corresponding waves; S_P and R_P denote the vector-separated P-wave of the source and receiver wavefields, respectively, and R_S denotes the vector-separated S-wave of the receiver wavefield; θ_P denotes the incident or reflected angle of the P-wave; and θ_S denotes the reflected angle of the S-wave. We obtain the following expressions $S_P\cdot R_P = |S_P||R_P|\cos(180°-2\theta_P)$ and $S_P\cdot R_S = |S_P||R_S|\cos(90°+\theta_P+\theta_S)$.

magnitude of the included angle between the vibration directions of the incident and reflected P-waves. Therefore, the reflector events of the PP image have a consistent sign distribution for a certain incident angle range $2\theta_P \in [0, +90°]$, but there is a sign change beyond this range. Consequently, this sign change (polarity reversal) may also damage the PP imaging quality, especially in the shallow zone, when multiple-shot PP migration images are stacked. Fortunately, the P-wave incident angle is available, and this problem can naturally be avoided by correcting or muting the image amplitudes at large incident angles ($|\theta_P| > 45°$) in the common-source domain.

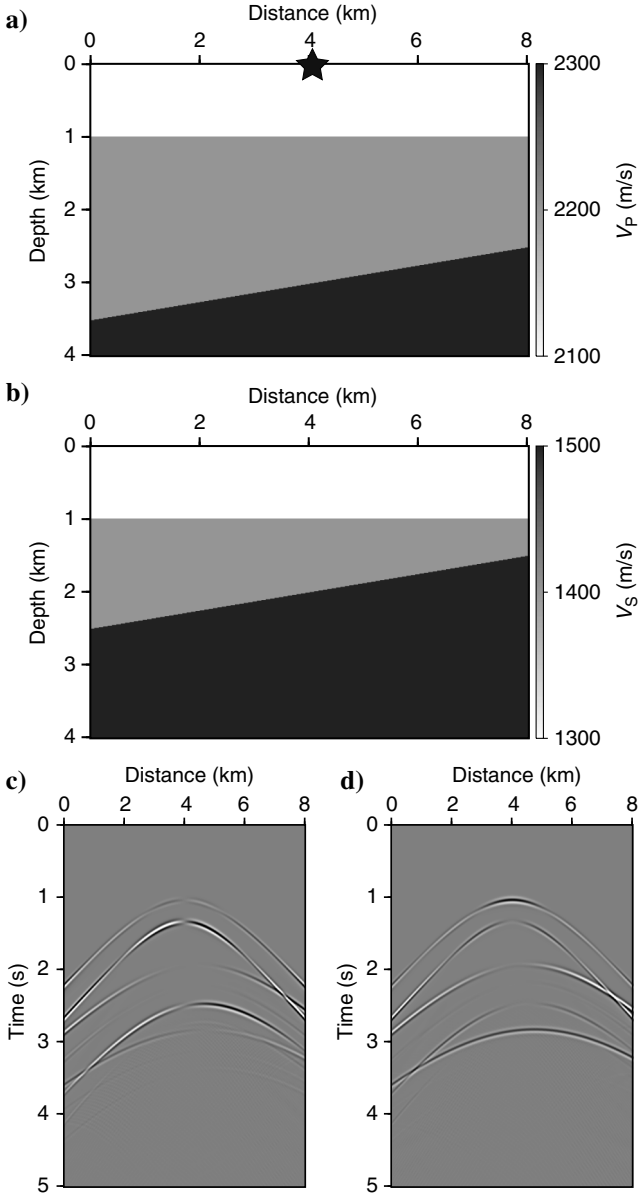

Figure 3. (a and b) The P- and S-wave velocity models with a flat reflector and a slant reflector, respectively. The star symbol denotes the pure P-wave source position. (c and d) The horizontal and vertical particle velocity seismic data, respectively, recorded at all surface grid points.

- For equation 12, the numerator for the PS reflection image can be transformed into the equation $S_P \cdot R_S = |S_P||R_S|\cos(90° + \theta_P + \theta_S) = -\sin(\theta_P + \theta_S)$, where θ_S denotes the S-wave reflected angle. It is evident from the equation that the sign of the PS reflection image constructed with equation 12 relies on the value of the included angle between the vibration directions of the incident P-wave and reflected S-wave. Because the angle $(\theta_P + \theta_S)$ is always less than 180°, the reflector events of the PS image have a consistent sign distribution over the entire P-wave incident angle range. Therefore, there is no requirement for the polarity-reversal correction in the proposed imaging condition of the PS reflection image.

Our previous interpretations for the inner-product imaging condition assumed that the PP and PS reflection coefficients were positive. In the same way, we can also obtain the interpretations for the proposed imaging condition, when the reflection coefficients are negative. To address the polarity-reversal problem of the PP image for the proposed imaging condition at large incident angles ($|\theta_P| > 45°$), another available solution is to find a scalar PP reflection image without polarity reversal (sign change) as a substitution for equation 11. The auxiliary P-wave stress τ^P in equation 10, which is a scalar wavefield similar to the pressure in the acoustic wave equation, presents the possibility of producing a better scalar image without the polarity-reversal problem. The source-normalized crosscorrelation imaging condition for the 2D P-wave stress image, for a common-source gather, is

$$I_{\mathrm{PP}^\tau}(x,z) = \frac{\sum_{it=1}^{nt} S_{\tau^P}(x,z,it) R_{\tau^P}(x,z,it)}{\sum_{it=1}^{nt} S_{\tau^P}^2(x,z,it)}, \qquad (13)$$

where $S_{\tau^P}(x,z,t)$ and $R_{\tau^P}(x,z,t)$ are the auxiliary P-wave stresses of the source and receiver wavefields, respectively, and I_{PP^τ} denotes the P-wave stress image (PP^τ image). The physical meaning of the PP^τ image can be interpreted in a similar way to the PP reflection image, and it can be considered a supplement or by-product when elastic RTM is performed with the proposed inner-product imaging condition.

NUMERICAL EXAMPLES

In this section, synthetic examples using a layered model, the Marmousi 2 model, and a fault model are used to evaluate three kinds of elastic imaging conditions. These elastic imaging conditions will produce unwanted low-frequency migration artifacts when the migration velocity model contains sharp velocity contrasts (Douma et al., 2010). Therefore, in the following examples, we use the smoothed velocity as the migration velocity to remove the low-frequency artifacts caused by secondary reflections and mode conversions produced by coupling at reflectors.

Layered velocity model

In the first example, we use the layered velocity model with a flat reflector and a slant reflector to demonstrate the advantages of the proposed imaging condition. The P- and S-wave velocity models with different slant reflectors are shown in Figure 3a and 3b. The density is set constant at 2000 kg/m^3. The grid numbers of the elastic model along the horizontal and vertical directions are

800 and 400, respectively. The grid size is 10×10 m. The source signature is a Ricker wavelet with a dominant frequency of 10 Hz, which is excited at (4 km, 0). Figure 3c and 3d displays the horizontal and vertical components of the synthetic multicomponent seismic data recorded on all surface grids. The maximum observed time is 5 s with a time step of 1 ms.

Figures 4, 5, and 6 display the single-shot migration images for the layered velocity model using the component-based, potential-based, and inner-product imaging conditions, respectively. The black rows in Figures 5b and 6a indicate the positions where polarity reversal occurred for the corresponding migration images. From these migration images, we make the following observations and analysis:

- Figure 4 displays the migration images using the component-based imaging condition (equations 2 and 3). The P- and S-wave velocity variations are present at the reflection event locations of the component-based images because the scattered P- and S-waves caused by the velocity variations are imaged in the component-based images simultaneously. The imaging quality of the horizontal-component migration image shown in Figure 4a is worse than of the vertical-component migration image shown in Figure 4b because the energy of the horizontal component is commonly weaker than that of the vertical component.
- Figure 5 displays the migration images with fewer artifacts and clearer events using the potential-based imaging condition (equations 4, 5, and 8) compared with the component-based migration images. However, the PS image in Figure 5b

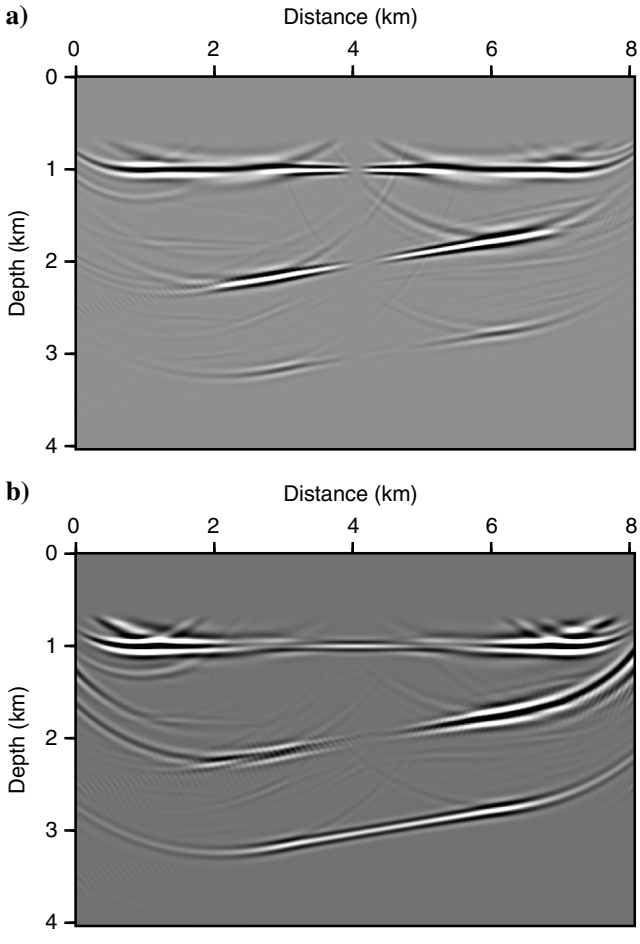

Figure 4. Single-shot elastic RTM images for the layered velocity model using the component-based imaging condition. (a and b) The horizontal- and vertical-component images, respectively.

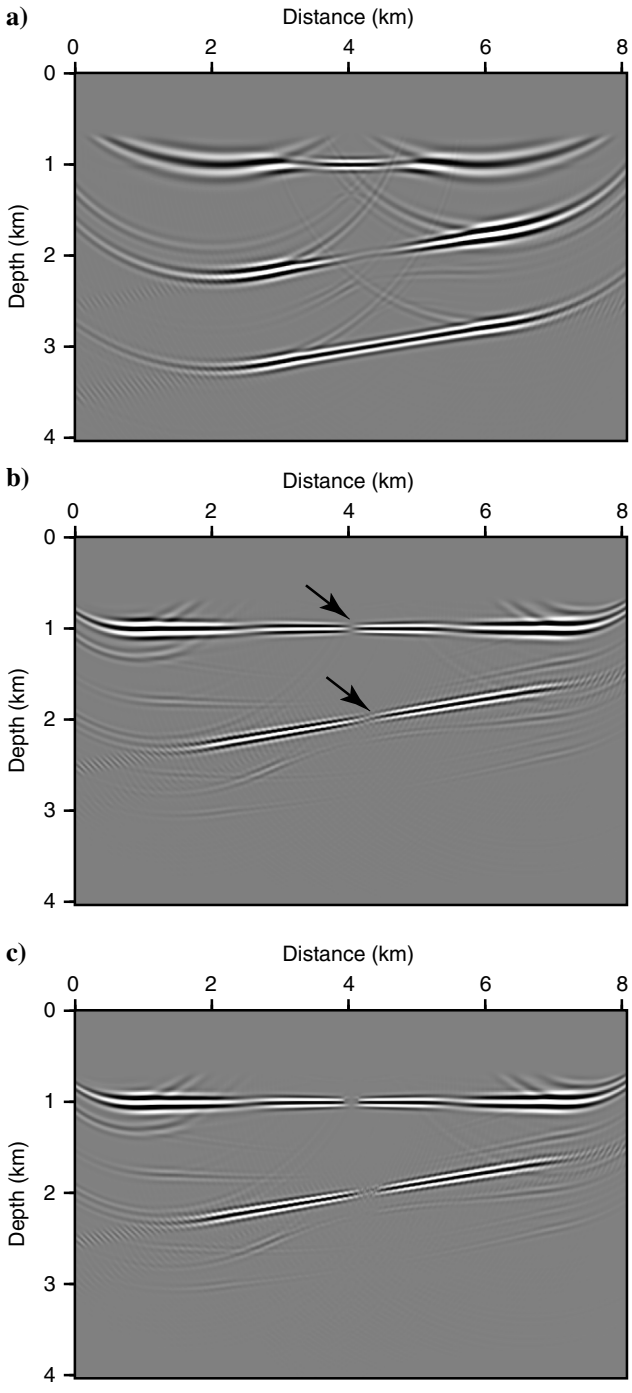

Figure 5. Single-shot elastic RTM images for the layered velocity model using the potential-based imaging condition: (a) the PP image, (b) the PS image without the polarity-reversal correction, and (c) the PS image with the polarity-reversal correction. The black rows indicate the locations where the polarity reversal occurred.

exhibits the polarity-reversal phenomenon, which is presented by the black rows. For the slant reflector, polarity reversal occurs at the nonzero offset. After application of the polarity-reversal correction, the reflector events of the PS reflection image shown in Figure 5c have a consistent sign distribution, which confirms the validity of our polarity-reversal correction approach for simple geologic conditions.

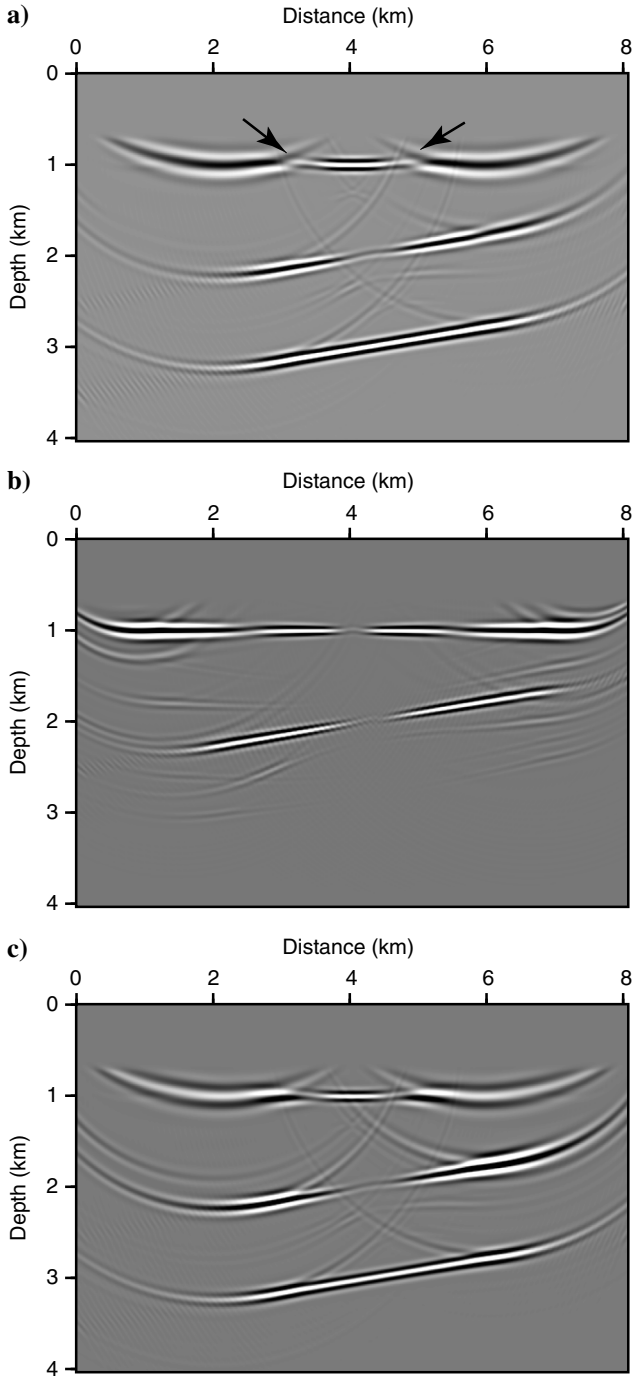

Figure 6. Single-shot elastic RTM images for the layered velocity model: (a) the PP image, (b) the PS image using the inner-product imaging condition, and (c) the PP$^{\tau}$ image. The black rows indicate the locations where the polarity reversal occurred.

- Figure 6 displays the migration images obtained by the inner-product (equations 11 and 12) and crosscorrelation imaging conditions (equation 13). We note that the PS image shown in Figure 6b has no polarity-reversal problem, but the PP image shown in Figure 6a has the flipped-polarity problem at the first reflector, which is consistent with our previous explanation for the proposed imaging condition. The black rows in Figure 6a show the position of the polarity reversal, which occurred at a large P-wave incident angle of $|\theta_P| > 45°$. The PP$^{\tau}$ image, which is displayed in Figure 6c, presents a high-quality reflectivity image with the correct amplitude, phase attributes, and no flipped polarity. Hence, in practice, the PP$^{\tau}$ image can be considered as a substitute or supplement for the PP reflectivity image when elastic RTM is performed with the proposed inner-product imaging condition.
- The PP images obtained by the potential-based and inner-product imaging conditions, which are shown in Figures 5a and 6a, appear to be structurally equivalent. We see from the two kinds of PP images that their phase difference is π, which can be attributed to the $\pi/2$ phase shift of the separated waves for the potential-based imaging condition in the source and receiver wavefields. Similarly, this phenomenon can be also discovered in the PS images obtained by the potential-based imaging condition with the polarity-reversal correction and the inner-product imaging condition, which are shown in Figures 5c and 6b, respectively.
- One interesting phenomenon is that all the PS images are free from the slant reflector of the P-wave velocity, but the S-wave velocity anomaly is present in the PP and PP$^{\tau}$ migration images. The reason for this phenomenon in the radiation patterns of the velocity-density parameterization is that the P-wave velocity variation only produces the PP-wavefield and the S-wave velocity variation can scatter PP- and PS-wavefields for an incident P-wavefield (Forgues and Lambaré, 1997). Therefore, the crosstalk artifacts between the two velocities occur only for the PP-wavefield, which can lead to the reflection of the S-wave velocity variation in the reflection events of the PP and PP$^{\tau}$ images. To remove the false reflection events in the PP image, the inversion-based elastic imaging approaches, such as elastic least-squares RTM (Duan et al., 2017; Feng and Schuster, 2017; Gu et al., 2017; Ren et al., 2017), combined with the decoupled elastic wave equation, need to be developed to further enhance the elastic imaging quality. However, this is beyond the scope of this paper.

Figure 7 compares the vertical profiles of the migration images shown in Figures 4–6 at 3.8 km along the horizontal direction. Figure 7a and 7b displays the vertical profiles of Figure 4a and 4b, respectively, Figure 7c–7e displays the vertical profiles of Figure 5a–5c, respectively, and Figure 7f–7h displays the vertical profiles of Figure 6a–6c, respectively. The phase information of the horizontal- and vertical-component images (displayed in Figure 7a and 7b, respectively) can be considered the standard for the other migration images because the horizontal and vertical components of the particle velocity are considered as the original input wavefields for performing an imaging condition. The vertical profiles of the PP, PS, and PP$^{\tau}$ images (displayed in Figure 7f–7h, respectively) obtained by the proposed imaging condition keep the original phase information, but the phase of the PP and PS images

(displayed in Figure 7c and 7e, respectively) obtained by the potential-based imaging condition are both shifted by π because the calculations of the divergence and curl operator involve spatial derivatives, which induce a $\pi/2$ phase shift. From these comparisons and observations, we conclude that the proposed imaging condition is superior to the potential-based imaging condition because

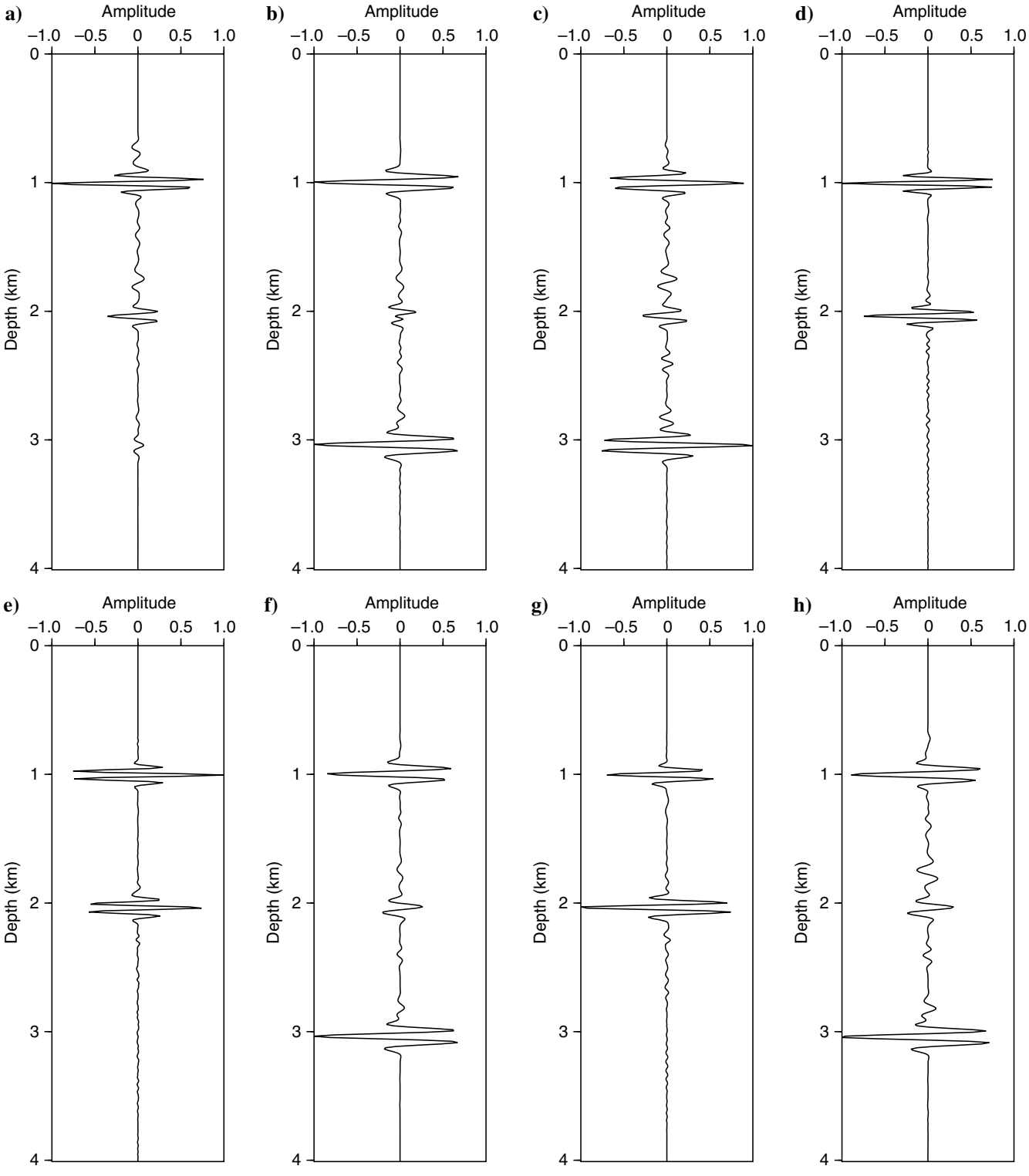

Figure 7. The vertical profiles of the migration images shown in Figures 4–6 at 3.8 km along the horizontal direction: (a) the horizontal- and (b) vertical-component images shown in Figure 4a and 4b, respectively; (c) the PP image, (d) the PS image, and (e) the PS image shown in Figure 5a–5c, respectively; (f) the PP image, (g) the PS image, and (h) the PP$^{\tau}$ image shown in Figure 6a–6c, respectively.

it produces migration images with better amplitude performance and preserved phase information. Although the PP image obtained by our proposed imaging condition can exhibit a polarity reversal at large incident angles, the PP^r image can be considered to be a substitute or supplement for the PP reflection image.

Table 1 displays the computational time of the single-shot elastic RTM for the layered velocity model using the different imaging conditions. Our computation platform is an Intel workstation (Xeon E5-2630 2.3G) with an Nvidia graphic card of Tesla K10, where we use the graphic processing unit (GPU) to accelerate the elastic wavefield stimulation and the application of the imaging condition. Among the elastic imaging conditions, the component-based imaging condition costs the shortest computational time because there is no requirement to decompose the P- and S-waves. The potential-based imaging condition takes the longest computational time because the polarity-reversal correction scheme presented in this paper requires an additional numerical implementation of the elastic RTM for the local angle of the reflector. Compared with the component-based imaging condition, the proposed imaging condition only slightly increases the computational cost because it only requires numerically solving equation 10 for the vector-based wavefield decomposition. Therefore, the inner-product imaging condition is a desired and alternative imaging condition for elastic RTM in terms of computational efficiency and imaging quality.

Marmousi 2 model

In the second example, we use a portion of the Marmousi 2 model to evaluate and compare the three imaging conditions. This elastic model is discretized into 920 (in the horizontal direction) by 300 (in the vertical direction) grid points, with a spatial interval of 10 m. The true P- and S-wave velocities of the model with different geologic structures are exhibited in Figure 8a and 8b. The migration velocities of the P- and S-waves are exhibited in Figure 8c and 8d. The density is homogeneous with a value of 2000 kg/m^3. We evenly model a total of 92 shot gathers on the surface, with a spatial interval of 100 m. The signature of the explosive source is a Ricker wavelet with a dominant frequency of 10 Hz. At most, each source has 400 multicomponent receivers. The time step is 1 ms, with a total length of 6 s.

Figures 9, 10, and 11 display the migration images obtained by the component-based, potential-based, and inner-product imaging conditions, respectively. It is apparent from Figure 9 that both velocity anomalies of the P- and S-waves are present in the component-based migration images, which are the crosstalk artifacts of

Table 1. Computational time of the single-shot elastic RTM using the three kinds of imaging conditions for the layered model. Our computation platform is an Intel workstation (Xeon E5-2630 2.3G) with an Nvidia graphic card of Tesla K10, where we use the GPU to accelerate the elastic wavefield stimulation and the application of the imaging condition.

Imaging conditions	Computational time
Component-based	146 s
Potential-based	352 s
Inner-product	180 s

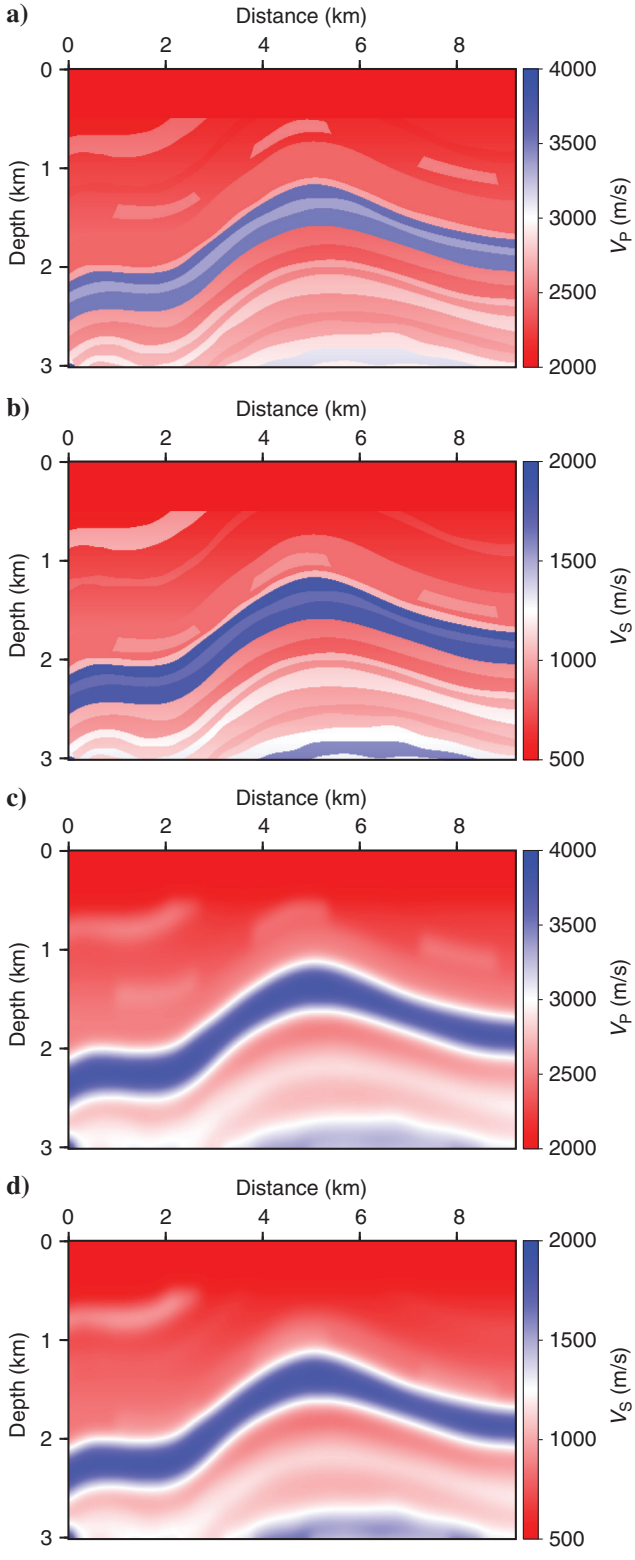

Figure 8. A portion of the Marmousi 2 model. (a and b) The true P- and S-wave velocity models, respectively. (c and d) The smoothed P- and S-wave velocity models, respectively.

the elastic RTM. The imaging quality of the potential-based migration images, which are displayed in Figure 10, is relatively better than that of the component-based migration images. However, the PS image without the polarity-reversal correction obtained by the potential-based imaging condition, which is shown in Figure 10b, has discontinuous reflection events and a lot of migration artifacts. This problem has been addressed by the polarity-reversal scheme described in this paper, which provides the improved PS imaging result shown in Figure 10c. The inner-product imaging condition provides high-quality PP and PS migration images, which are shown in Figure 11a and 11b, respectively. The PS images obtained by the polarity-reversal correction method and the proposed inner-product imaging condition present comparable reflectivity images with continuous and well-focused reflection events. However, the polarity-reversal correction method does not provide an accurate image amplitude because the separated waves used for the elastic imaging have altered the amplitude information of the input elastic wavefields. The PP image obtained by the inner-product imaging condition presents slightly weak imaging amplitudes at the shallow zone, which can be attributed to the polarity reversal of the PP image at large incident angles ($|\theta_P| > 45°$). But the PP^r image, which is displayed in Figure 11c, provides a supplement for the high-quality PP reflection image with strong imaging amplitudes at the shallow zone, compared with the PP reflection image using the inner-product imaging condition.

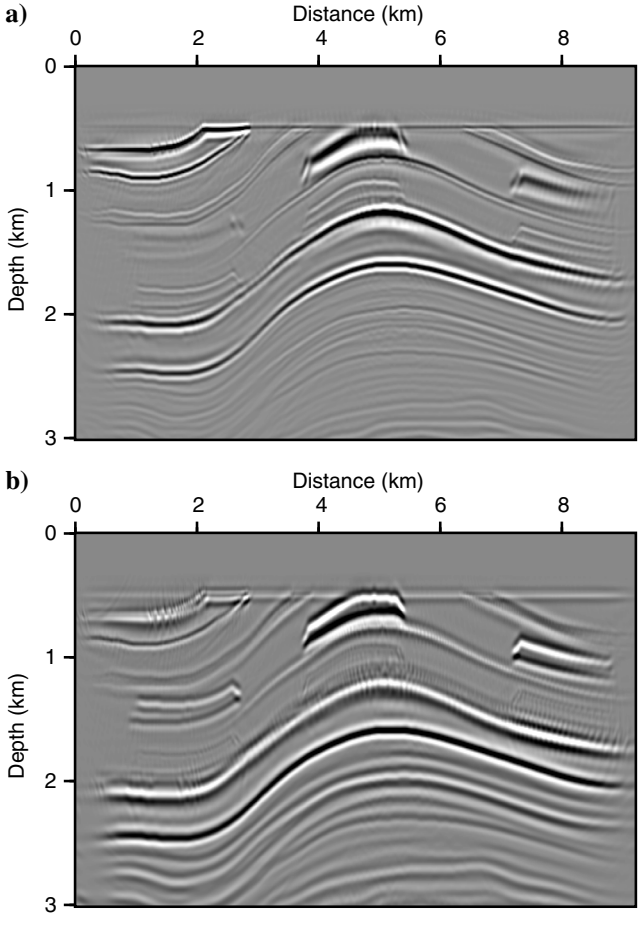

Figure 9. Elastic RTM images for the Marmousi 2 model using the component-based imaging condition: (a) the horizontal-component and (b) the vertical-component images.

Fault model

In the last example, we use the fault model to further evaluate the three kinds of imaging conditions. This fault model is discretized

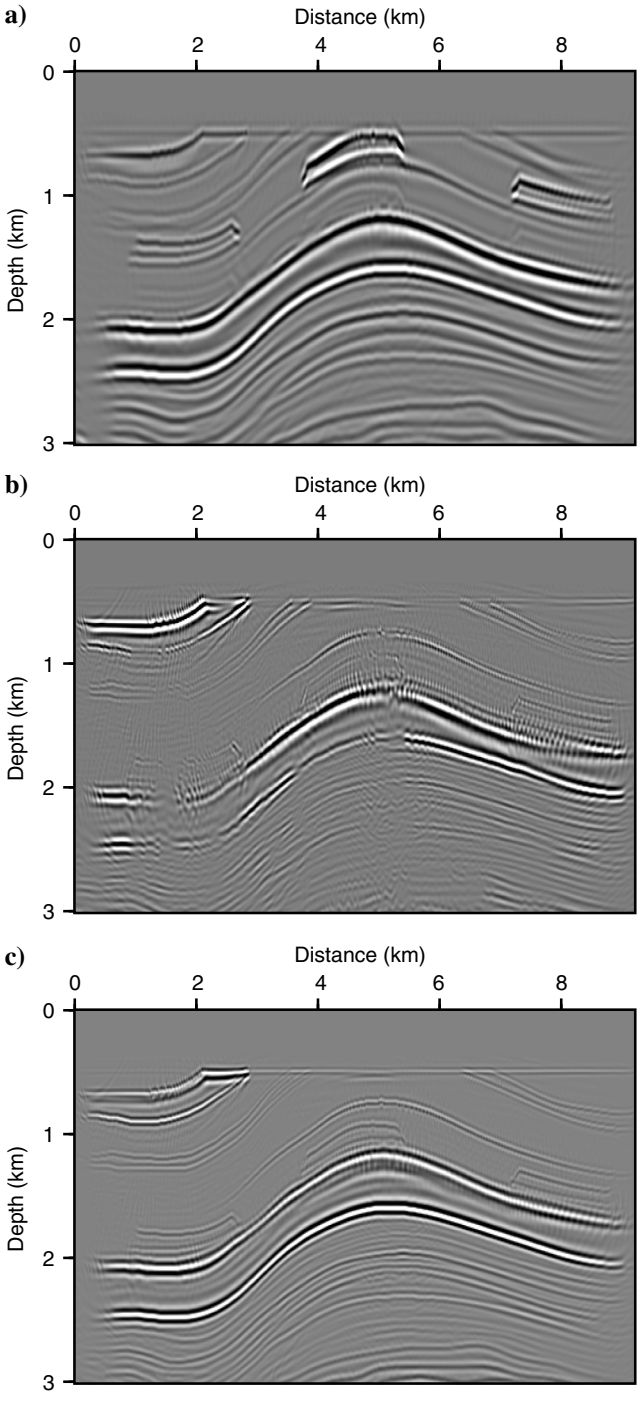

Figure 10. Elastic RTM images for the Marmousi 2 model using the potential-based imaging condition: (a) the PP image, (b) the PS image without the polarity-reversal correction, and (c) the PS image with the polarity-reversal correction.

into 1300 (in the horizontal direction) by 650 (in the vertical direction) grid points, with a spatial interval of 10 m. Figure 12a displays the true P-wave velocity of the model. The migration model presented in Figure 12b is produced by performing a Gaussian smooth filter with six wavelength window length on the true model. The true and migration velocity models of the S-wave are derived from the true and migration velocity models of the P-wave based on an empirical formula $V_S = V_P/\sqrt{3}$. The density is constant at 2000 kg/m^3. The explosive source is a Ricker wavelet with a dominant frequency of 15 Hz. We generated a total of 130 shot gathers along the surface starting from the left edge of the model. Each source with a spatial interval of 100 m has 600 receivers with a spatial interval of 10 m. The recording time is 8 s, with a time step of 1 ms.

Figures 13, 14, and 15 exhibit these multiple-shot stacked migration images for the component-based, potential-based, and inner-product imaging conditions, respectively. By comparing these migration images, we make the following observations and analysis:

- All migration images are capable of characterizing complex geologic structures, with the exception of the PS image in Figure 14b. The crosstalk artifacts of the migration images caused by the nonphysical and unseparated wave modes have been completely suppressed by multiple-shots stacking. The vertical resolutions of the PP, PP^r, and vertical-component images are lower than those of the images associated with the S-waves because the reflected P-waves have longer wavelengths than the converted S-waves.
- The PS image without the polarity-reversal correction obtained by the potential-based imaging condition, which is shown in Figure 14b, presents some discontinuous and unclear reflection events. After correcting the polarity reversal of the PS image from equation 8, the quality of the PS image shown in Figure 14c has some obvious improvements, but it is inferior to the quality of the PS image shown in Figure 15b obtained by the proposed inner-product imaging condition. The reason for this phenomenon is that the polarity correction scheme relying on the polarization vector in the time-space domain may become unreliable for complicated structures, and the proposed inner-product imaging condition for

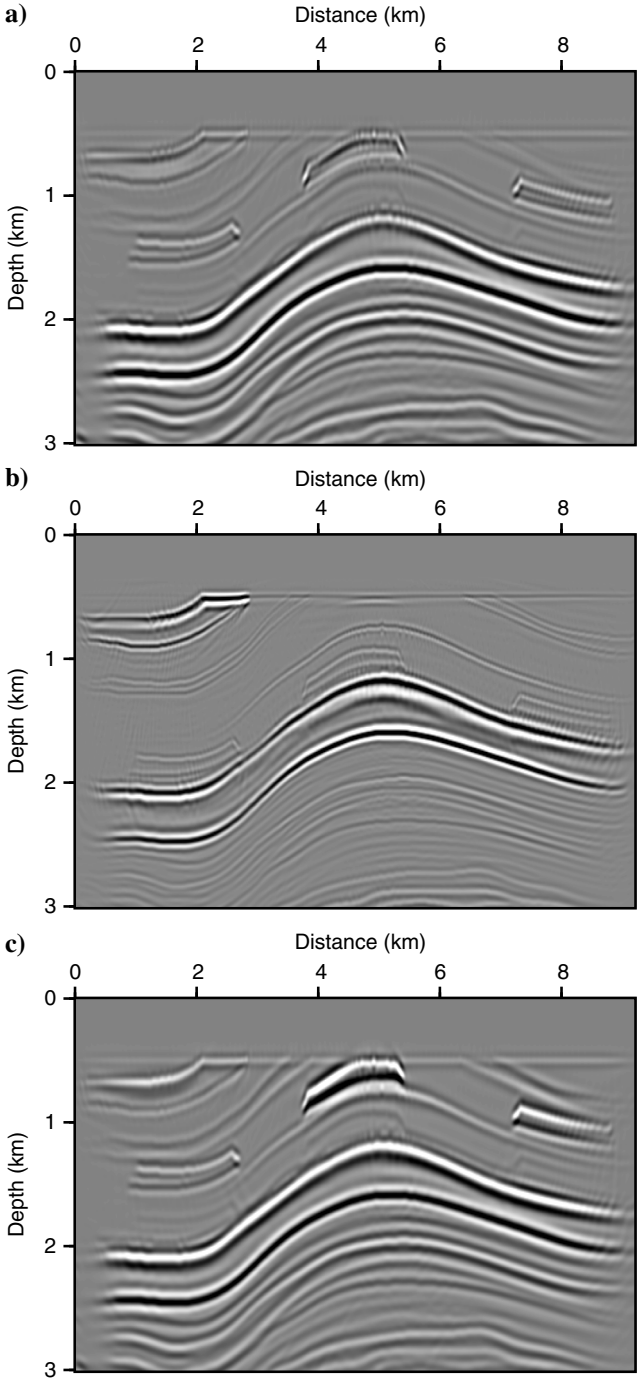

Figure 11. Elastic RTM images for the Marmousi 2 model: (a) the PP image, (b) the PS image using the inner-product imaging condition, and (c) the PP^r image.

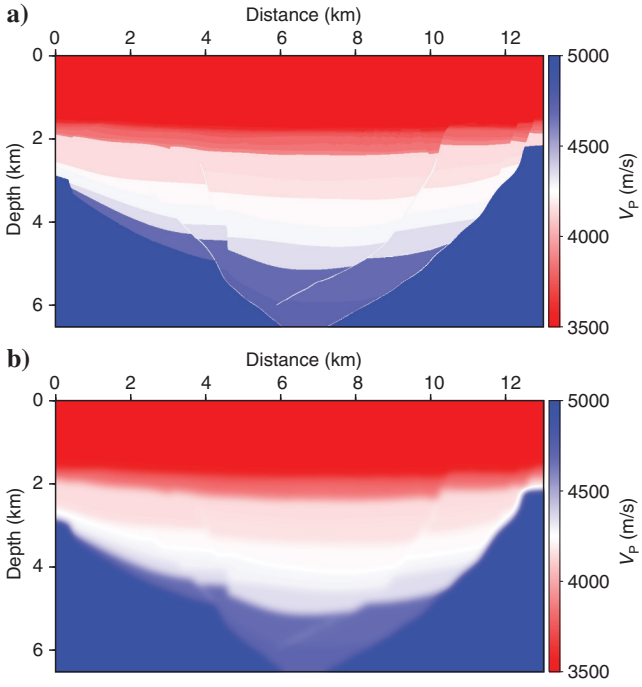

Figure 12. The P-wave velocity models of the elastic fault. (a and b) The true and smoothed velocity models, respectively.

the PS image is free from the polarity-reversal problem in arbitrary complicated structures.

- The PP images obtained by the potential-based and inner-product imaging conditions, which are shown in Figures 14a and 15a, respectively, and the PP^r image shown in Figure 15c appear to be structurally equivalent. We see from the two kinds of PP images that their phase difference is π, which is attributed to the $\pi/2$ phase shift of the separated waves for the potential-based imaging condition in the source and receiver wavefields. Similarly, this phenomenon can also be discovered in the PS images obtained by the potential-based and inner-product imaging conditions, which are shown in Figures 14c and 15b, respectively.

The magnified views for the migration images shown in Figures 13–15 are exhibited in Figures 16, 17, and 18, respectively. The magnified views presented in Figure 16 characterize the flat, dipping, and fault reflectors very well, but they have no clear physical meaning for interpreting the physical properties. The PS image shown in Figure 17b has the worst migration quality with destructive interference in the flat and dipping reflectors. The polarity-reversal correction approach for the PS image shown in Figure 17c provides improved imaging quality, but it is inferior to the quality of the PS image shown in Figure 18b obtained by the proposed inner-product imaging condition. Moreover, the PS image shown in Figure 17c has a few discontinuous events presented by the black rows, where the polarity-reversal correction method may become unreliable in the complicated structures at a large dip-angle. The magnified views in Figure 18 present the same phase information as Figure 16, which demonstrates that the proposed imaging condition has the capacity to preserve phase information. Moreover, they appear to be continuous and well-focused events with no flipped polarity. These observations and comparisons confirm that the proposed imaging condition is the most accurate and promising imaging condition for elastic RTM.

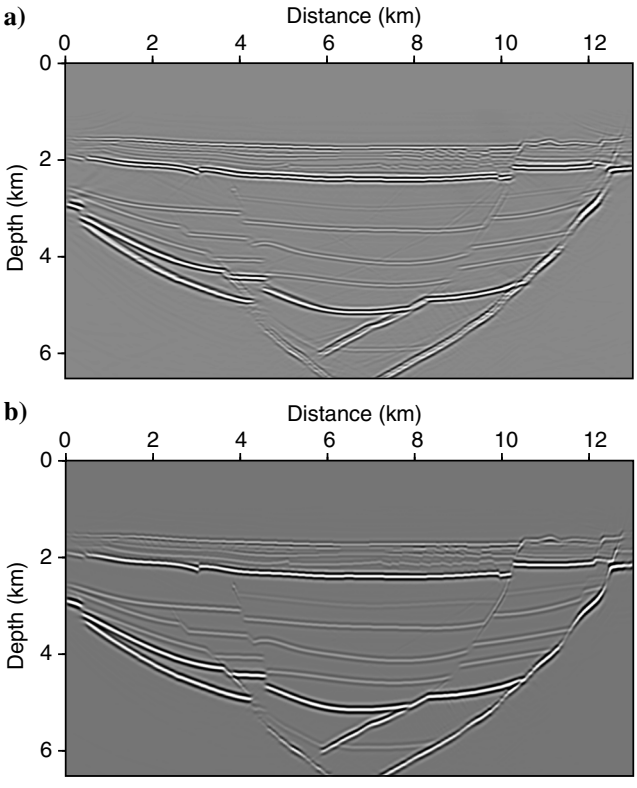

Figure 13. The migration images for the fault model using the component-based imaging condition: (a) the horizontal- and (b) vertical-component images.

DISCUSSION

We have successfully evaluated three kinds of imaging conditions for 2D elastic RTM. It is impossible to directly construct a scalar PS reflection image in the 3D case from the conventional potential-

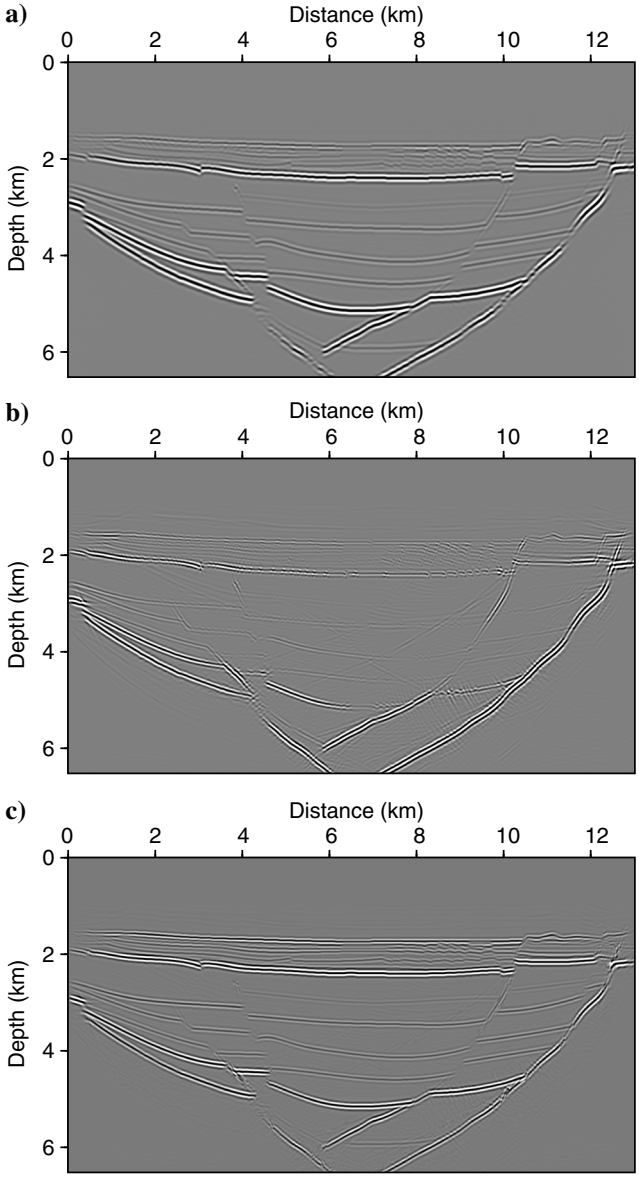

Figure 14. The migration images for the fault model using the potential-based imaging condition: (a) the PP image, (b) the PS image without the polarity-reversal correction, and (c) the PS image with the polarity-reversal correction.

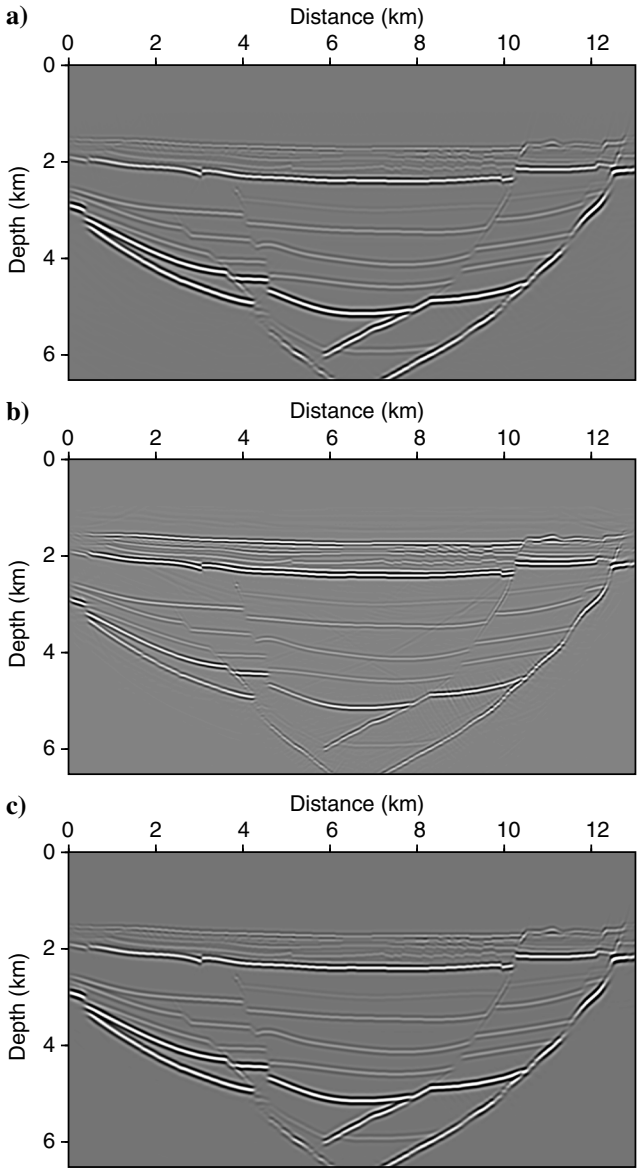

Figure 15. The migration images for the fault model: (a) the PP image, (b) the PS image using the inner-product and imaging condition, and (c) the PP^r image.

based imaging condition because the S-wave separated by the curl operator is a 3C vector and the P-wave separated by the divergence operator is a scalar quantity. Hence, the conventional potential-based imaging condition is hard to extend to the 3D case, unless the S-wave separated by the curl operator is scalarized by some special calculations (Du et al., 2014; Duan and Sava, 2015; Gong et al., 2018). Unlike the conventional potential-based imaging condition, the inner-product imaging condition between the vector-separated waves from the source and receiver wavefields can provide scalar reflection images of the subsurface without additional calculation. Therefore, our proposed inner-product imaging condition combined with the decoupled elastic wave equation, which is easy to extend to the 3D case and applicable to the field data, may provide satisfactory migration images for the elastic RTM. The P-wave stress image in equation 13 can be also extended to the 3D case and supplement the elastic imaging, when the elastic RTM is implemented with the inner-product imaging condition because the P-wave stress used for the elastic imaging is a scalar wavefield similar to the pressure in the acoustic-wave equation. The inner-product imaging condition can also be extended to incorporate more variables, such as attenuation (Zhu and Carcione, 2014) and anisotropy (Wang et al., 2016). Zhu and Sun (2017) propose a viscoelastic RTM approach with attenuation compensation, which uses the inner-product imaging condition between the vector-separated waves for imaging attenuated multicomponent seismic data. The imaging condition that directly uses the decomposed qP- and qS-waves for anisotropic RTM is currently under investigation (Wang et al., 2016). The vector-based P- and S-waves decomposition for the vertical and tilted transverse isotropic media requires solving the Christoffel equation (Zhang and McMechan, 2010; Wang et al., 2018b) at significantly greater expense. Cheaper and more accurate vector decomposition methods for anisotropic media need to be explored.

In general, for reducing the computational cost and getting better stability, the elastic RTM approach always applies the adjoint of the forward-modeling operator to obtain subsurface images, instead of the inverse operator. Zhu et al. (2009) and Luo et al. (2013) implement 2D and 3D elastic imaging based on the adjoint methods, respectively. In the elastic imaging approach, they use the sensitivity kernels as the imaging condition to produce images of subsurface structures. The implementation of the bulk-modulus sensitivity kernel in the adjoint imaging approach, which is equation 6 in Zhu et al. (2009) and equation 9 in Luo et al. (2013), is equal to the potential-based imaging condition for the PP reflection image

Figure 16. Magnified views of the migration images in Figure 13: (a) the horizontal-component and (b) the vertical-component images.

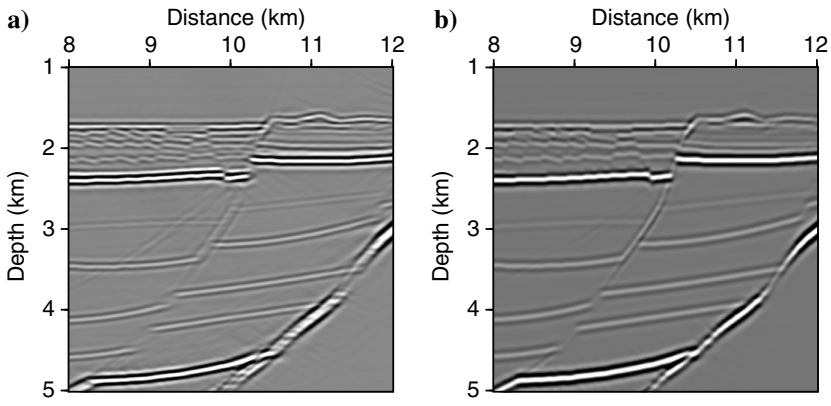

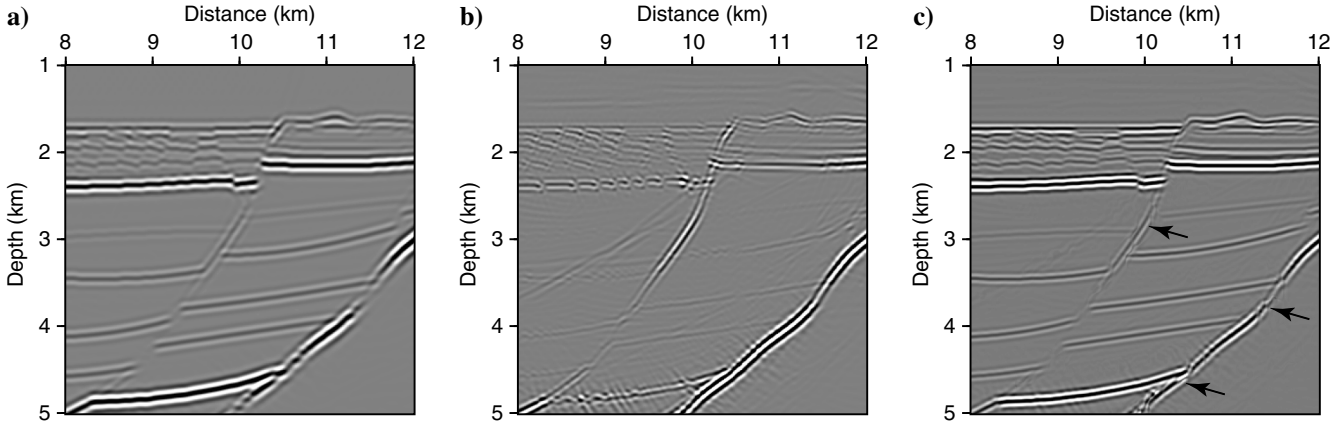

Figure 17. Magnified views of the migration images in Figure 14: (a) the PP image, (b) the PS image without the polarity-reversal correction, and (c) the PS image with the polarity-reversal correction. The black rows indicate the locations where the polarity-reversal correction method may become unreliable.

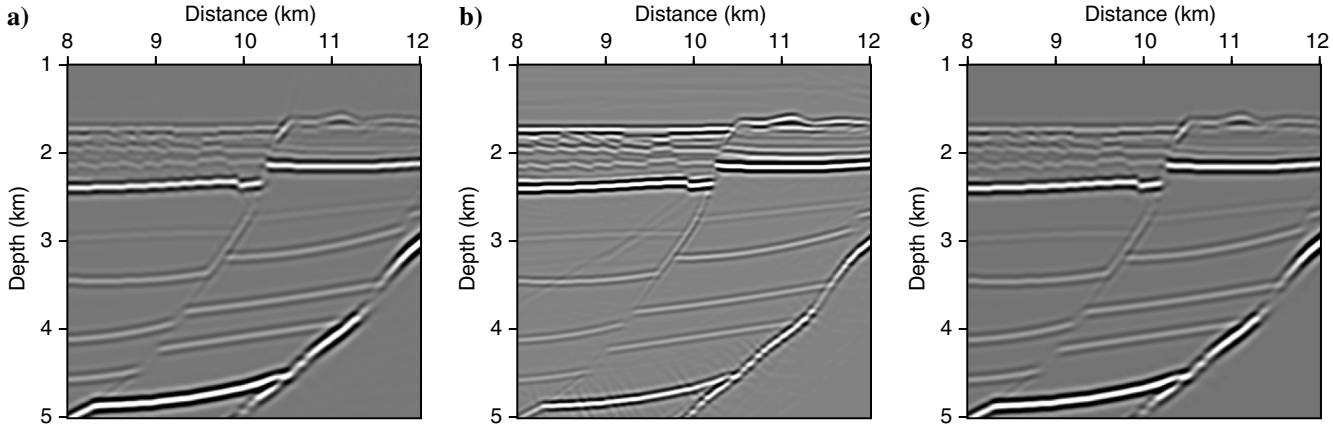

Figure 18. Magnified views of the migration images in Figure 15: (a) the PP image, (b) the PS image, and (c) the PP^{τ} image.

(equation 4), if we ignore the scaling factor $-\kappa$ (κ is the bulk modulus). However, we can easily see that the proposed inner-product imaging condition for the PP reflection image is different from the calculation of the bulk-modulus sensitivity kernel because we used the inner product between the vector-separated waves from the decoupled elastic wave equation to produce the migration image. Fortunately, the P-wave stress image in equation 13 is consistent with the calculation of the bulk-modulus sensitivity kernel, which can be interpreted as the PP reflection image because the P-wave stress wavefield in equation 10 is identical to the separated P-wave component assuming no scaling factor $\lambda + 2\mu$. Besides, the migrated image constructed by the bulk-modulus sensitivity kernel can be interpreted as the PP reflectivity image of the subsurface; the other sensitivity kernels provide the migrated images, which are not consistent with our understanding of seismic reflectivity. As a result, these migration images constructed with the shear-modulus and density sensitivity kernels only provide the high-wavenumber component of the subsurface model parameter, which are only suitable for characterizing the position of subsurface reflectors and difficult to interpret for physical properties of seismic reflectivity.

CONCLUSION

Three kinds of imaging conditions are presented and compared for imaging quality in elastic RTM: the component-based, potential-based, and inner-product imaging conditions. The component-based imaging condition produces subsurface images with serious crosstalk artifacts and unclear physical meaning, which are only suitable for characterizing subsurface structures. Although the potential-based imaging condition is capable of providing better imaging quality, the polarity-reversal problem leads to the destructive interference of the converted-wave image. The polarity-reversal correction scheme in the common-source domain is able to overcome this problem, but it is only suitable for simple geologic structures. The inner-product imaging condition is proposed for imaging vector-separated waves from the decoupled elastic wave equation to produce subsurface images. The main advantage of the imaging condition is that the PS reflection image is free from the polarity-reversal problem. The P-wave stress image can supplement or take the place of the PP reflection image when elastic RTM is implemented with the proposed imaging condition. Synthetic examples

with a layered model, the Marmousi 2 model, and a fault model have demonstrated that the inner-product imaging condition has more advantages and can retrieve subsurface images with better amplitude performance.

ACKNOWLEDGMENTS

The authors are grateful for the support of the National Natural Science Foundation of China (grant nos. 41574117 and 41474118), Heilongjiang Province Natural Science Fund for Distinguished Young Scholar (grant no. JC2016006), and Northeast Petroleum University Excellent Scientific Talent Fund (grant no. GLJHB201601). We also thank D. Draganov, J. Schleicher, and the anonymous reviewers for their valuable suggestions and comments.

DATA AND MATERIALS AVAILABILITY

Data associated with this research are available and can be obtained by contacting the corresponding author.

REFERENCES

Aki, K., and P. G. Richards, 1980, Quantitative seismology, theory and methods: W. H. Freeman and Co.

Berenger, J. P., 1994, A perfectly matched layer for the absorption of electromagnetic waves: Journal of Computational Physics, **114**, 185–200, doi: 10.1006/jcph.1994.1159.

Chang, W. F., and G. A. McMechan, 1986, Reverse-time migration of offset vertical seismic profiling data using the excitation-time imaging condition: Geophysics, **51**, 67–84, doi: 10.1190/1.1442041.

Chang, W. F., and G. A. McMechan, 1987, Elastic reverse-time migration: Geophysics, **52**, 1365–1375, doi: 10.1190/1.1442249.

Chang, W. F., and G. A. McMechan, 1994, 3D elastic prestack reverse-time depth migration: Geophysics, **59**, 597–609, doi: 10.1190/1.1443620.

Chattopadhyay, S., and G. A. McMechan, 2008, Imaging conditions for prestack reverse-time migration: Geophysics, **73**, no. 3, S81–S89, doi: 10.1190/1.2903822.

Claerbout, J. F., 1971, Toward a unified theory of reflector mapping: Geophysics, **36**, 467–481, doi: 10.6038/cjg20130323.

Douma, H., D. Yingst, I. Vasconcelos, and J. Tromp, 2010, On the connection between artifact filtering in reverse-time migration and adjoint tomography: Geophysics, **75**, no. 6, S219–S223, doi: 10.1190/1.3505124.

Du, Q. Z., X. Gong, M. Zhang, Y. Zhu, and G. Fang, 2014, 3D PS-wave imaging with elastic reverse-time migration: Geophysics, **79**, no. 5, S173–S184, doi: 10.1190/GEO2013-0253.1.

Du, Q. Z., C. F. Guo, Q. Zhao, X. F. Gong, C. X. Wang, and X. Y. Li, 2017, Vector-based elastic reverse time migration based on scalar imaging condition: Geophysics, **82**, no. 2, S111–S127, doi: 10.1190/GEO2016-0146.1.

Du, Q. Z., Y. Zhu, and J. Ba, 2012, Polarity reversal correction for elastic reverse time migration: Geophysics, **77**, no. 2, S31–S41, doi: 10.1190/geo2011-0348.1.

Duan, Y. T., A. Guitton, and P. Sava, 2017, Elastic least-squares reverse time migration: Geophysics, **82**, no. 4, S315–S325, doi: 10.1190/geo2016-0564.1.

Duan, Y. T., and P. Sava, 2015, Scalar imaging condition for elastic reverse time migration: Geophysics, **80**, no. 4, S127–S136, doi: 10.1190/geo2014-0453.1.

Feng, Z. C., and G. T. Schuster, 2017, Elastic least-squares reverse time migration: Geophysics, **82**, no. 2, S143–S157, doi: 10.1190/GEO2016-0254.1.

Forgues, E., and G. Lambaré, 1997, Parameterization study for acoustic and elastic ray + Born inversion: Journal of Seismic Exploration, **6**, 253–278.

Gong, T., B. Nguyen, and G. A. McMechan, 2016, Polarized wavefield magnitudes with optical flow for elastic angle-domain common-image gathers: Geophysics, **81**, no. 4, S239–S251, doi: 10.1190/GEO2015-0518.1.

Gong, X., Q Du, and Q. Zhao, 2018, SP- and SS-imaging for 3D elastic reverse time migration: Geophysics, **83**, no. 1, A1–A6, doi: 10.1190/GEO2017-0286.1.

Gu, B. L., Z. Li, and X. Ma, 2015, Multi-component elastic reverse time migration based on the P- and S-wave separated velocity-stress equations: Journal of Applied Geophysics, **112**, 62–78, doi: 10.1016/j.jappgeo.2014.11.008.

Gu, B. L., Z. C. Li, P. Yang, W. C. Xu, and J. G. Han, 2017, Elastic least-squares reverse time migration with hybrid l_1/l_2 misfit function: Geophysics, **82**, no. 3, S271–S291, doi: 10.1190/GEO2016-0235.1.

Hokstad, K., 2000, Multicomponent Kirchhoff migration: Geophysics, **65**, 861–873, doi: 10.1190/1.1444783.

Jin, H., G. A. McMechan, and B. Nguyen, 2015, Improving I/O performance in 2D and 3D ADCIGs from RTM: Geophysics, **80**, no. 2, S65–S77, doi: 10.1190/GEO2014-0209.1.

Kaelin, B., and A. Guitton, 2006, Imaging condition for reverse time migration: 76th Annual International Meeting, SEG, Expanded Abstracts, 2594–2598, doi: 10.1190/1.2370059.

Kuo, J. T., and T. F. Dai, 1984, Kirchhoff elastic wave migration for the case of noncoincident source and receiver: Geophysics, **49**, 1223–1238, doi: 10.1190/1.1441751.

Li, Z., X. Ma, C. Fu, and G. Liang, 2016, Wavefield separation and polarity reversal correction in elastic reverse time migration: Journal of Applied Geophysics, **127**, 56–67, doi: 10.1016/j.jappgeo.2016.02.012.

Lowenthal, D., and L. Hu, 1991, Two methods for computing the imaging condition for common-shot prestack migration: Geophysics, **56**, 378–381, doi: 10.1190/1.1443053.

Luo, Y., J. Tromp, B. Denel, and H. Calandra, 2013, 3D coupled acoustic-elastic migration with topography and bathymetry based on spectral-element and adjoint methods: Geophysics, **78**, no. 4, S193–S202, doi: 10.1190/geo2012-0462.1.

Ma, D., and G. Zhu, 2003, P- and S-wave separated elastic wave equation numerical modeling (in Chinese): Oil Geophysical Prospecting, **38**, 482–486, doi: 10.1190/1.2792904.

Nguyen, B., and G. A. McMechan, 2013, Excitation amplitude imaging condition for prestack reverse-time migration: Geophysics, **78**, no. 1, S37–S46, doi: 10.1190/GEO2012-0079.1.

Nguyen, B., and G. A. McMechan, 2015, Five ways to avoid storing source wavefield snapshots in 2D elastic prestack reverse-time migration: Geophysics, **80**, no. 1, S1–S8, doi: 10.1190/geo2014-0014.1.

Ren, Z. M., Y. Liu, and M. K. Sen, 2017, Least-squares reverse time migration in elastic media: Geophysical Journal International, **208**, 1103–1125, doi: 10.1093/gji/ggw443.

Rosales, D., S. Fomel, B. Biondi, and P. Sava, 2008, Wave-equation angle-domain common-image gathers for converted waves: Geophysics, **73**, no. 1, S17–S26, doi: 10.1190/1.2821193.

Rosales, D., and J. Rickett, 2001, PS-wave polarity reversal in angle domain common-image gathers: 71st Annual International Meeting, SEG, Expanded Abstracts, 1843–1846, doi: 10.1190/1.2370059.

Schleicher, J., J. C. Costa, and A. Novais, 2008, A comparison of imaging conditions for wave-equation shot-profile migration: Geophysics, **73**, no. 6, S219–S227, doi: 10.1190/1.2976776.

Shi, Y., and Y. Wang, 2016, Reverse time migration of 3D vertical seismic profile data: Geophysics, **81**, no. 1, S31–S38, doi: 10.1190/geo2015-0277.1.

Sun, R., J. Chow, and K. J. Chen, 2001, Phase correction in separating P and S-waves in elastic data: Geophysics, **66**, 1515–1518, doi: 10.1190/1.1487097.

Sun, R., and G. A. McMechan, 1986, Pre-stack reverse-time migration for elastic waves with application to synthetic offset vertical seismic profiles: Proceedings of the IEEE, **74**, 457–465, doi: 10.1109/PROC.1986.13486.

Sun, R., and G. A. McMechan, 2001, Scalar reverse-time depth migration of prestack elastic seismic data: Geophysics, **66**, 1519–1527, doi: 10.1190/1.1487098.

Sun, R., G. A. McMechan, and H. Chuang, 2011, Amplitude balancing in separating P- and S-waves in 2D and 3D elastic seismic data: Geophysics, **76**, no. 3, S103–S113, doi: 10.1190/13555529.

Virieux, J., 1986, P-SV wave propagation in heterogeneous media: Velocity-stress finite-difference method: Geophysics, **51**, 889–901, doi: 10.1190/1.1442147.

Wang, C., J. Cheng, and B. Arntsen, 2016, Scalar and vector imaging based on wave mode decoupling for elastic reverse time migration in isotropic and transversely isotropic media: Geophysics, **81**, no. 5, S383–S398, doi: 10.1190/geo2015-0704.1.

Wang, G., S. Wang, J. Song, C. Dong, and M. Zhang, 2018a, Elastic reflection traveltime inversion with decoupled wave equation: Geophysics, **83**, no. 5, R463–R474, doi: 10.1190/geo2017-0631.1.

Wang, W., B. Hua, G. A. McMechan, and B. Duquet, 2018b, P- and S-decomposition in anisotropic media with localized low-rank approximations: Geophysics, **83**, no. 1, C13–C26, doi: 10.1190/GEO2017-0138.1.

Wang, W., and G. A. McMechan, 2015, Vector-based elastic reverse time migration: Geophysics, **80**, no. 6, S245–S258, doi: 10.1190/geo2014-0620.1.

Wang, W., G. A. McMechan, and Q. Zhang, 2015, Comparison of two algorithms for isotropic elastic P and S decomposition in the vector domain: Geophysics, **80**, no. 4, T147–T160, doi: 10.1190/geo2014-0563.1.

Wang, W. H., W. Zhang, Y. Shi, and X. Ke, 2017, Elastic reverse time migration based on wavefield separation: Chinese Journal of Geophysics, **60**, 554–568, doi: 10.6038/cjg20170726.

Wu, R. S., 1994, Wide-angle elastic wave one-way propagation in heterogeneous media and an elastic wave complex-screen method: Journal of Geophysical Research, **99**, 751–766, doi: 10.1029/93JB02518.

Xiao, X., and W. S. Leaney, 2010, Local vertical seismic profiling (VSP) elastic reverse-time migration and migration resolution: Salt-flank imaging with transmitted P-to-S waves: Geophysics, **75**, no. 2, S35–S49, doi: 10.1190/1.3309460.

Xie, X. B., and R. S. Wu, 2005, Multicomponent prestack depth migration using the elastic screen method: Geophysics, **70**, no. 10, S30–S37, doi: 10.1190/1.1852787.

Yan, J., and T. A. Dickens, 2016, Reverse time migration angle gathers using Poynting vectors: Geophysics, **81**, no. 6, S511–S522, doi: 10.1190/GEO2015-0703.1.

Yan, J., and P. Sava, 2008, Isotropic angle-domain elastic reverse-time migration: Geophysics, **73**, no. 6, S229–S239, doi: 10.1190/1.2981241.

Zhang, J., Z. Tian, and C. Wang, 2007, P- and S-wave-separated elastic wave equation numerical modeling using 2D staggered-grid: 77th Annual International Meeting, SEG, Expanded Abstracts, 2104–2109, doi: 10.1190/1.2792904.

Zhang, Q., and G. A. McMechan, 2010, 2D and 3D elastic wavefield vector decomposition in the wavenumber domain for VTI media: Geophysics, **75**, no. 3, D13–D26, doi: 10.1190/1.3431045.

Zhang, Q., and G. A. McMechan, 2011, Direct vector-field method to obtain angle-domain common-image gathers from isotropic acoustic and elastic reverse time migration: Geophysics, **76**, no. 5, WB135–WB149, doi: 10.1190/geo2010-0314.1.

Zhu, H., Y. Luo, T. Nissen-Meyer, C. Morency, and J. Tromp, 2009, Elastic imaging and time-lapse migration based on adjoint methods: Geophysics, **74**, no. 6, WCA167–WCA177, doi: 10.1190/1.3261747.

Zhu, T., and J. M. Carcione, 2014, Theory and modeling of constant-Q P- and S-waves using fractional spatial derivatives: Geophysical Journal International, **196**, 1787–1795, doi: 10.1093/gji/ggt483.

Zhu, T., and J. Sun, 2017, Viscoelastic reverse time migration with attenuation compensation: Geophysics, **82**, no. 2, S61–S73, doi: 10.1190/geo2016-0239.1.